

Supporting Information

Remote p-d Orbital Hybridization via First/Second-layer Coordination of Fe Single Atoms with Heteroatoms for Enhanced Electrochemical CO₂-to-CO Reduction

Ying Yang, Lizhen Chen, Zhenyan Guo, Shengqi Liu, Pei-dong Wu, Zhen Fang, Kai Zhang,* Hu Li**

1. Experimental Section

1.1 Materials

All chemicals used were of analytical grade and used directly without further purification. Zinc nitrate hexahydrate ($\text{Zn}(\text{NO}_3)_2 \cdot 6\text{H}_2\text{O}$, $\geq 99.0\%$), ferrous sulfate heptahydrate ($\text{FeSO}_4 \cdot 7\text{H}_2\text{O}$, $\geq 99.0\%$), thiourea (99%), melamine (≥ 99.05), dimethylimidazole ($\geq 98\%$), methanol ($\geq 99.5\%$), *N,N*-dimethylformamide (DMF, $\geq 99.5\%$), potassium bicarbonate (KHCO_3 , $\geq 99.5\%$), potassium thiocyanate (KSCN, 99%) and Nafion solutions (5 wt%) were purchased from Shanghai Aladdin Biochemical Technology Co., Ltd. Ion exchange membrane (Nafion[®] 115) was purchased from Dupont. The electrolyte solution was prepared by using deionized water (18.25 M Ω).

1.2 Catalyst Synthesis

Synthesis of (S)/Fe-ZIF-8: Zinc nitrate hexahydrate (1.78 g) and ferrous sulfate heptahydrate (48.4 mg) were stirred vigorously to be dissolved in 100 mL of methanol (A solution). Likewise, dimethylimidazole (1.94 g) and thiourea (150 mg) were added into 80 mL methanol and completely dissolved under stirring conditions (600 rpm) (B solution). Then, A solution was gradually injected into the B solution and treated at 60 °C for 24 h. The precipitated solid was separated by centrifugation, and rinsed three times using methanol, followed by drying overnight at 80 °C. The procedure for preparing Fe-ZIF-8 was identical to that for S/Fe-ZIF-8, but without using thiourea.

Synthesis of (S)/Fe-ZIF-8-M: (S)/Fe-ZIF-8 (0.4 g) and melamine (0.2 g) were dispersed in *N,N*-dimethylformamide (10 mL) and thermo-treated at 60 °C for 3 h, and then undergoing sonication for 1 h. The obtained mixture was subsequently transferred to a vacuum oven for drying to finally obtain S/Fe-ZIF-8-M. S/Fe-ZIF-8-M1 was obtained using the same method except that the amount of melamine increased from 0.2 g to 0.4 g. In addition, Fe-ZIF-8-M was synthesized utilizing the same procedures as for S/Fe-ZIF-8-M, except that no thiourea was added.

Synthesis of (S)/Fe-poN₄-C(C1): The above-prepared (S)/Fe-ZIF-8-M(M1) sample was kept at 1100 °C for 3 h under nitrogen protection (10 mL·min⁻¹) at a ramp rate of 5 °C per minute. Upon completion, the obtained sample was etched with 0.5 M H₂SO₄ at 60 °C to afford the target electrocatalyst, denoted as S/Fe-poN₄-C, S/Fe-poN₄-C1, or Fe-poN₄-C.

Synthesis of (S)/Fe-pdN₄-C: The (S)/Fe-ZIF-8 samples were kept at 1100 °C for 3 h in a nitrogen atmosphere (10 mL·min⁻¹) at a ramp rate of 5 °C per minute. After cooling to room temperature, the attained solid was etched with 0.5 M H₂SO₄ at 60 °C to furnish S/Fe-pdN₄-C or S/Fe-pdN₄-C.

1.3 Electrochemical measurements

CO₂ electroreduction (CO₂ER) measurements were carried out on the CHI 760E electrochemical analyzer. The catalyst ink was prepared by adding 5 mg catalyst to 490 μL of ethanol and 10 μL of Nafion solution (5 wt%) and subjected to sonication for 1 h. Then, 100 μL of the catalyst ink was dispersed onto a pretreated carbon cloth (1.0 × 1.0 cm²), which was dried at 80 °C for 30 min. The catalyst loading was 0.98 mg·cm⁻². The reference electrode was Ag/AgCl (Saturated with 3.5 M KCl) and the counter electrode was a Pt plate. All potentials were referenced to the reversible hydrogen electrode (RHE) with the equation of $E(vs. RHE) = E(Ag/AgCl) + 0.196 + 0.059 \times pH$. A three-electrode H-type electrolytic cell separated by Nafion 117 proton exchange membrane was used within a CO₂-saturated 0.5 M KHCO₃ solution (pH = 7.2). Prior to the measurement for CO₂RR performance, the electrolyte was purified with high-purity CO₂ (99.999%) for at least 30 min. Linear sweep voltammetry (LSV) was performed with a scan rate of 10 mV·s⁻¹ in CO₂ and N₂-saturated 0.5 M KHCO₃ aqueous electrolyte. Electrochemical impedance spectroscopy (EIS) was measured with the frequency range of 100000 - 0.1 Hz at different overpotentials. Before the reaction, the impurities adsorbed on the catalyst surface were removed by scanning the CV. The gaseous products for CO₂RR were quantified by online gas chromatography (GC, FULL

GC9790 II) with TCD and FID detectors, while liquid products of CO₂ER were detected via ¹H nuclear magnetic resonance (NMR) (Agilent, DD₂ 600 MHz). The electrochemically active surface area (ECSA) for each Fe-N₄ catalyst was determined by assessing the electrochemical double-layer capacitance (C_{dl}) of the catalyst surface. Cyclic voltammograms (CVs) were acquired within the voltage range of 0.75-0.85 V (vs. RHE), where the recorded current response exclusively stemmed from the charging of the double layer. Subsequently, C_{dl} was computed by analyzing the slope of a linear fit generated from plots of current density at 0.80 V against the scan rate. Tafel curves were obtained by determining the relationship between log|J_{CO}| and overpotential for each Fe-N₄ catalyst. After determining the position of the linear segment in the Tafel curve by second-order differentiation (i.e., the position of the second-order differentiation is 0), the Tafel slope was obtained by linearly fitting the selected segment.

The Faradaic efficiency was calculated by the following equation:

$$FE = \frac{Q_i}{Q_{total}} = \frac{ZnF}{Q_{total}} \times 100$$

Q_{total} : charge passed the electrode (C)

Q_i : charge used for the formation of products (C)

Z: number of electrons transferred (CO was 2)

n : moles of products (mol)

F: Faraday constant (96485 C/mol)

TOF calculations: The TOF was calculated through the following equation.¹

$$TOF(h^{-1}) = \frac{I_{CO}/ZF}{\omega \times m_{cat}/M_{Fe}} \times 3600$$

I_{CO} : CO partial current density (A)

Z: number of electrons transferred (CO was 2)

F: Faradaic constant (96485 C/mol)

m_{cat} : mass of as-prepared catalyst on carbon paper (g)

ω : Fe loading rate of catalyst (wt%)

M_{Fe} : relative atomic mass of Fe (55.8 g/mol).

1.4 Electrochemical measurements in flow cell

The performance of the cathode was evaluated by the constant potential method in a flow cell. The cathode and anode chambers were separated by an ion exchange membrane (Nafion® 115, Dupont). Ni foam was used as the anode and Ag/AgCl electrode as the reference electrode. The cathode is an as-prepared catalyst loaded on a gas diffusion layer (GDL). The flow rate of the electrolyte (1 M KOH) in both the cathode and anode chambers was set to 20 mL min⁻¹. CO₂ gas was delivered at an average rate of 20 mL min⁻¹. The preparation procedure of the cathodic gas diffusion electrode (GDE): The homogeneous ink was prepared by dispersing 24 mg catalyst and 50 µL Nafion solution (5 wt%) in 3 mL isopropanol and then the catalyst ink was uniformly sprayed onto the carbon fiber paper with 3.0 × 3.0 cm². Specifically, ensure that the catalyst load is 0.98 mg·cm⁻².

1.5 Physical characterization

The crystal structure of the samples was examined using a Bruker D8 X-ray diffractometer (XRD) (Cu K α radiation, $\lambda = 1.54 \text{ \AA}$, RIGAKU). Raman spectra were obtained using a laser micro-Raman spectrometer (Renishaw InVia, UK). Scanning electron microscope (SEM) images were collected from the TESCAN MIRA3 field emission scanning electron microscope (LMH). The morphology of the samples was characterized by transmission electron microscopy (TEM) (FEI TALOS F200X) with an accelerating voltage of 200 kV. The aberration-corrected high-angle annular dark-field STEM (AC HAADF-STEM) images were acquired using Titan 80-300 and Titan Cubed Themis 60-300 scanning/transmission electron microscopes operating at 300 kV, equipped with probe spherical aberration correctors. The metal content of the samples was tested by an inductively coupled plasma instrument (ICP-OES 730, Agilent) after microwave digestion. The elemental composition and chemical state of the samples were analyzed by an X-ray photoelectron spectrometer (XPS, Thermo Scientific ESCALAB 250Xi) with an Al anode target X-ray source. The content of the N

atom and S atom was tested by CHNS. The XPS test was run under a voltage of 16 kV and a current of 15 mA. X-ray absorption fine structure spectroscopy (XAFS) data reduction and analysis were processed by the Athena software. The catalyst functional groups were determined by KBr compression using Nicolet 360 FT-IR (Fourier-transform infrared) apparatus.

1.6 Computational details

The Vienna Ab Initio Package (VASP) was employed to perform all the density functional theory (DFT) calculations within the generalized gradient approximation (GGA) using the Perdew, Burke, and Enzerhof (PBE) formulation.²⁻⁴ The projected augmented wave (PAW) potentials were applied to describe the ionic cores and take valence electrons into account using a plane wave basis set with a kinetic energy cutoff of 520 eV.^{5, 6} Partial occupancies of the Kohn-Sham orbitals were allowed using the Gaussian smearing method and a width of 0.05 eV. The electronic energy was considered self-consistent when the energy change was smaller than 10^{-5} eV. A geometry optimization was considered convergent when the force change was smaller than 0.05 eV/Å. Grimme's DFT-D3 methodology was used to describe the dispersion interactions.⁷ And the S/Fe-pdN₄-C, Fe-pdN₄-C, S/Fe-poN₄-C, and Fe-poN₄-C had been used the $2 \times 2 \times 1$ Monkhorst-Pack k-point. The free energy was calculated as follows:

$$G = E + ZPE - TS$$

where G, E, ZPE, and TS are the free energy, total energy from DFT calculations, zero point energy, and entropic contributions, respectively. The U correction had been used in our structures for Fe metal atoms (4.93 eV).

1.7 In situ attenuated total reflectance surface-enhanced infrared absorption spectroscopy (ATR-SEIRAS) measurements.

ATR-SEIRAS was performed on a Nicolet is50 FT-IR spectrometer with an MCT detector, which was cooled by liquid nitrogen during the test.⁸⁻¹¹ A silicon semi-cylindrical prism (diameter: 20 mm) coated with gold and the prepared electrocatalyst

was used as the working electrode. The Ag/AgCl and Pt wire were used as the reference electrode and the counter electrode, respectively. ATR-SEIRAS was recorded on CO₂-saturated 0.5 M KHCO₃ by stepwise switching the potential from OCP to -0.98 V. The spectrum collected at the open circuit voltage was used for the background subtraction.

2. Supplementary Figures and tables

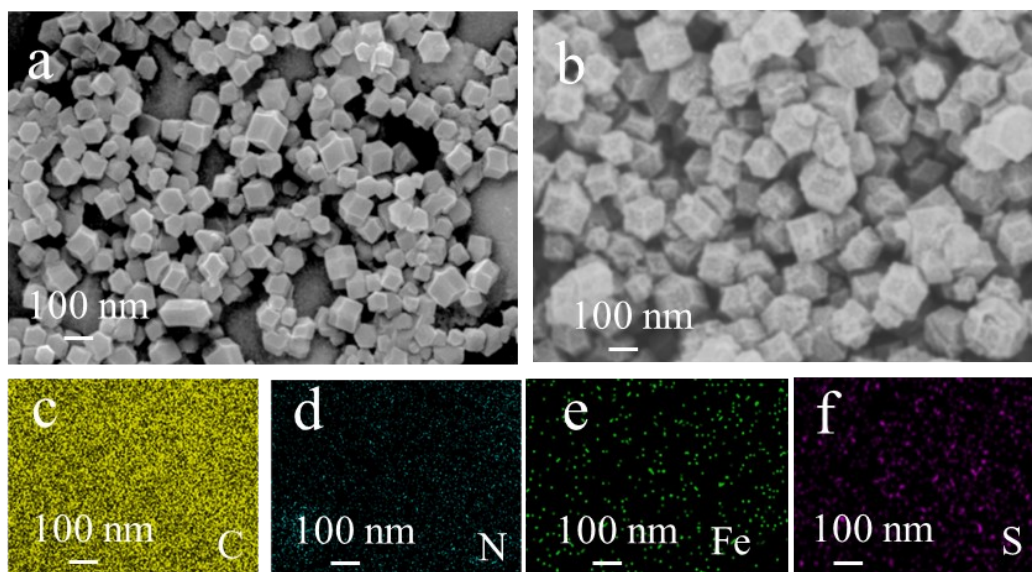


Figure S1. SEM images of S/Fe-ZIF-8 (a), and S/Fe-pdN₄-C (b). (c-f) Elemental mappings of S/Fe-pdN₄-C.

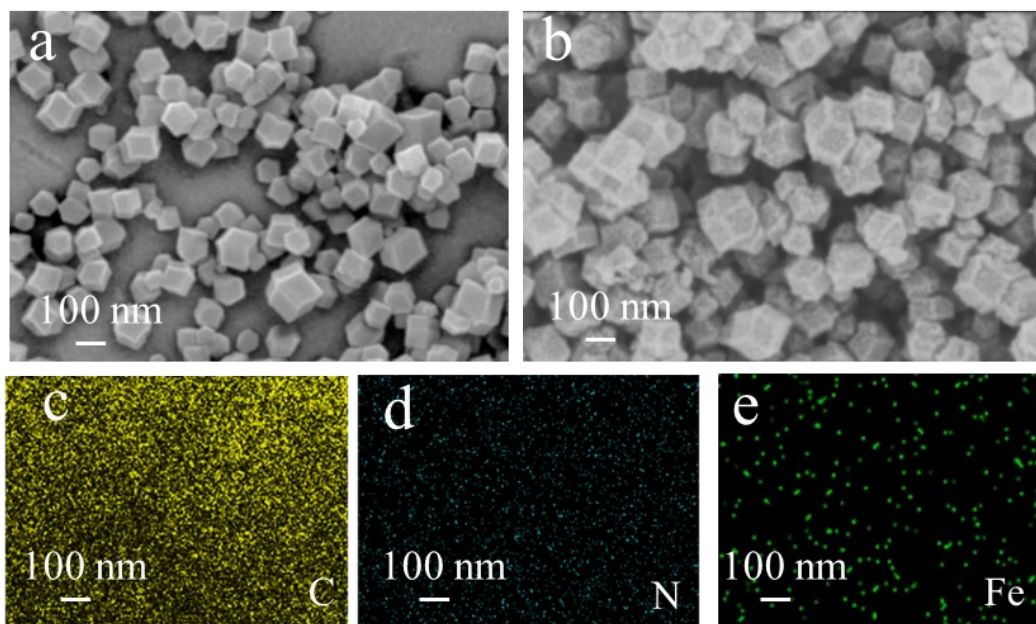


Figure S2. SEM images of Fe-ZIF-8 (a), and Fe-pdN₄-C (b). (c-e) Elemental mappings of Fe-pdN₄-C.

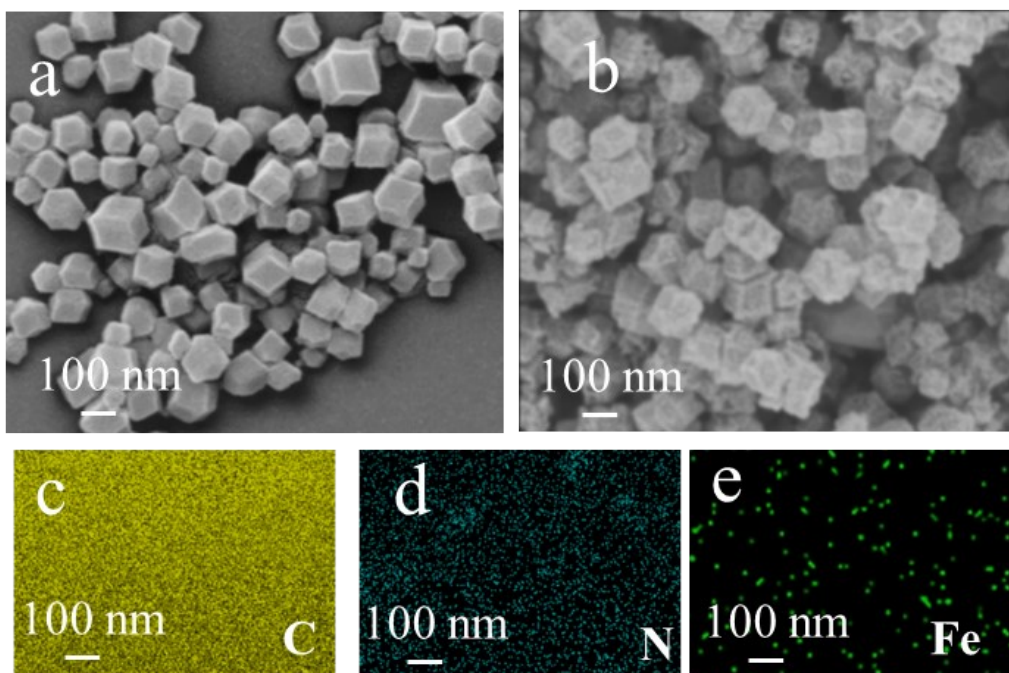


Figure S3. SEM images of Fe-ZIF-8-M (a), and Fe-poN₄-C (b). (c-e) Elemental mappings of Fe-poN₄-C.

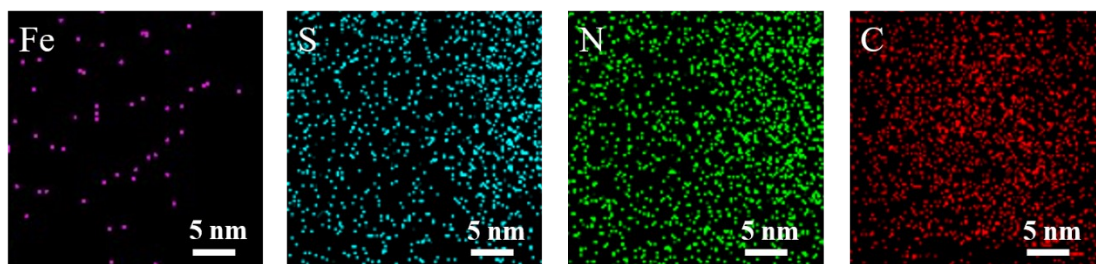


Figure S4. AC-HAADF-STEM EDS element mappings of S/Fe-poN₄-C.

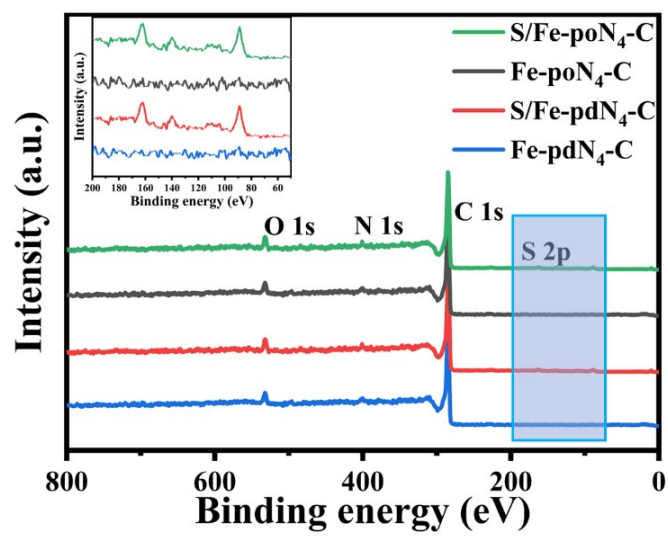


Figure S5. Full XPS survey spectra of different Fe-N₄ electrocatalysts.

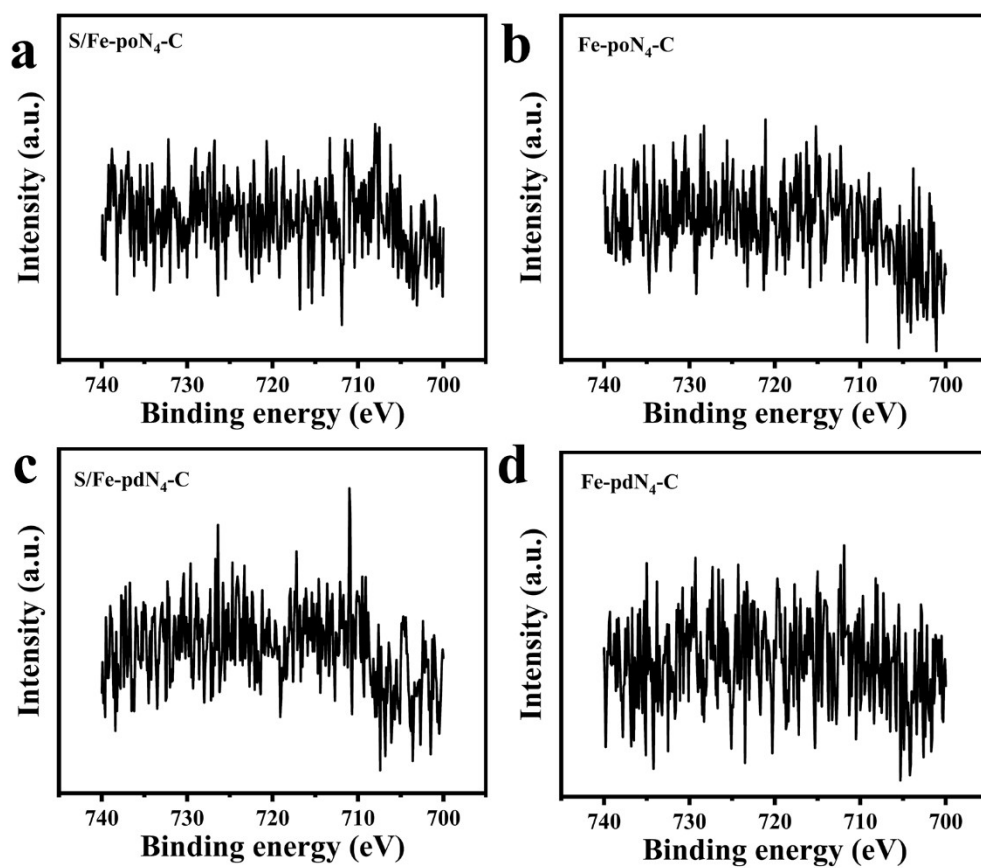


Figure S6. Fe 2p XPS spectra of a) S/Fe-poN₄-C, b) Fe-poN₄-C, c) S/Fe-pdN₄-C, and d) Fe-pdN₄-C.

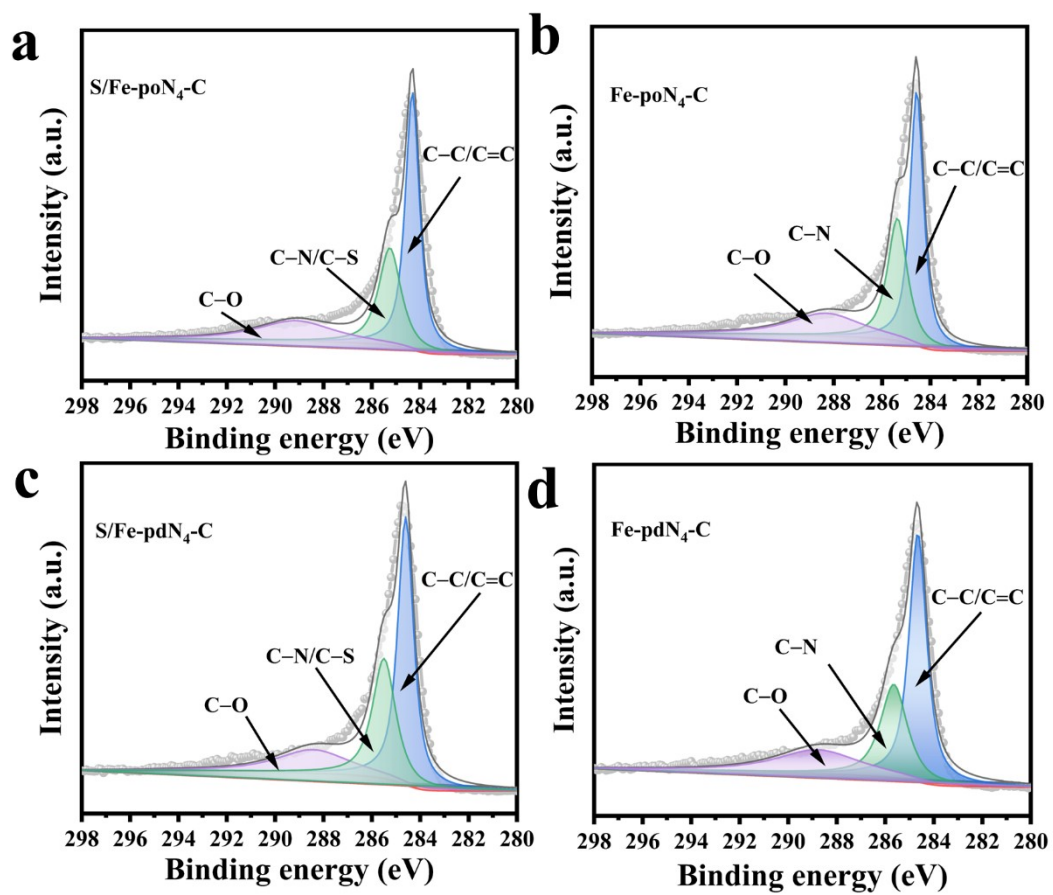


Figure S7. C 1s XPS spectra of a) S/Fe-poN₄-C, b) Fe-poN₄-C, c) S/Fe-pdN₄-C, and d) Fe-pdN₄-C.

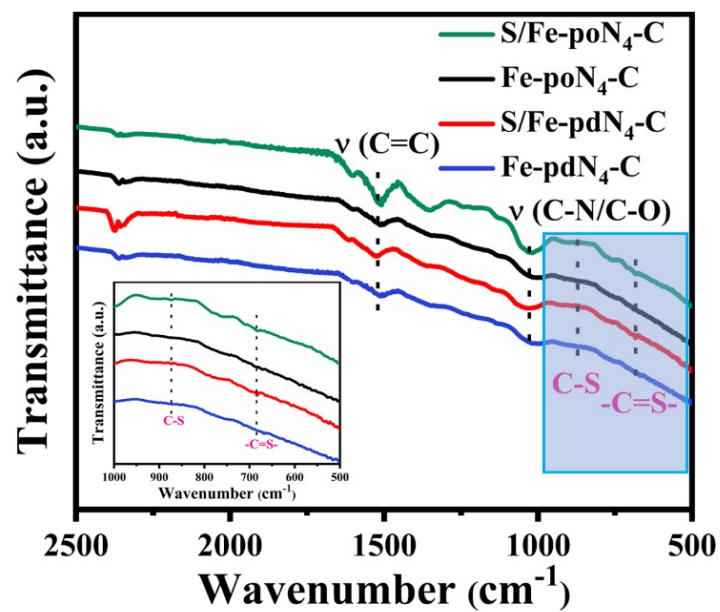


Figure S8. FT-IR spectra of S/Fe-poN₄-C, Fe-poN₄-C, S/Fe-pdN₄-C, and Fe-pdN₄-C.

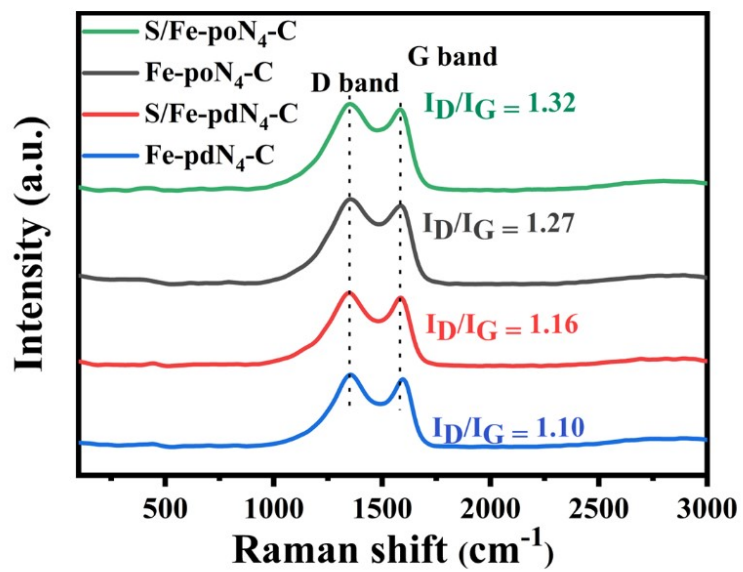


Figure S9. Raman spectra of S/Fe-poN₄-C, Fe-poN₄-C, S/Fe-pdN₄-C, and Fe-pdN₄-C.

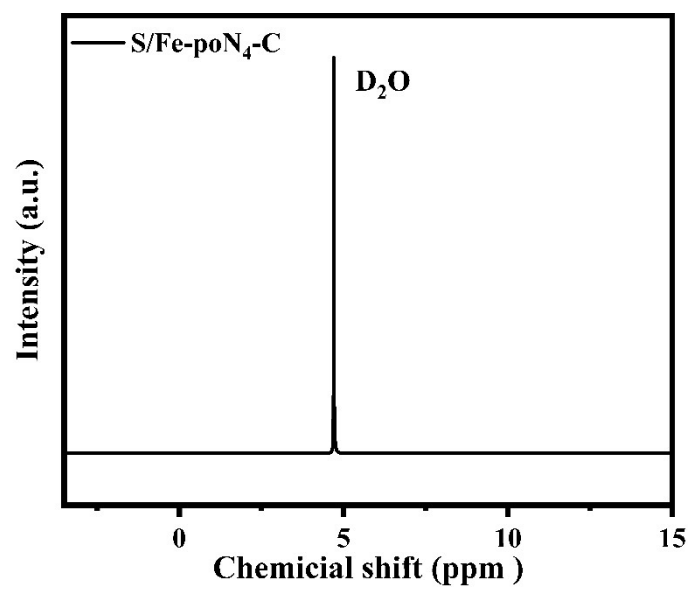


Figure S10. ¹H-NMR spectrum of the electrolyte after CO₂RR at -0.58 V using S/Fe-poN₄-C.

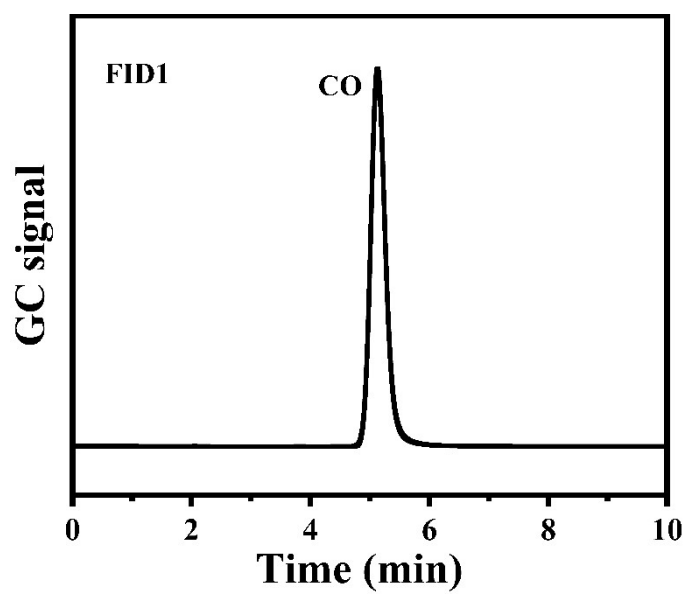


Figure S11. The CO signal peak of S/Fe-poN₄-C was detected by gas chromatography at -0.58 V.

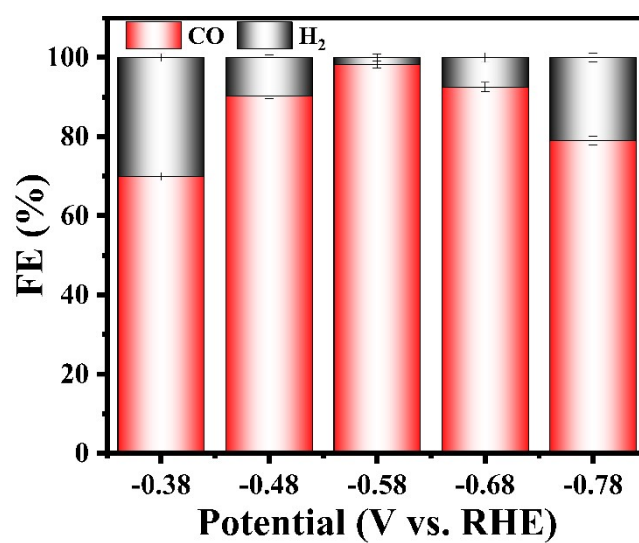


Figure S12. Faraday efficiency (FE) of S/Fe-poN₄-C for CO and H₂ at the varied potentials.

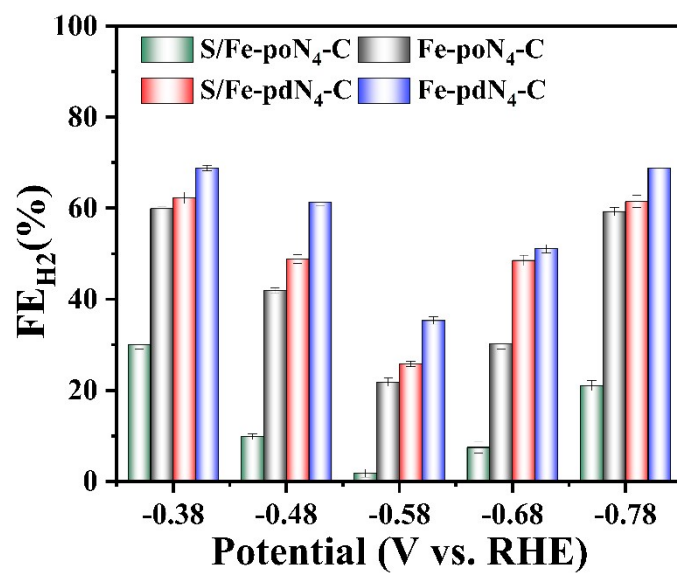


Figure S13. Faraday efficiency for hydrogen (FE_{H₂}) of S/Fe-poN₄-C, Fe-poN₄-C, S/Fe-pdN₄-C, and Fe-pdN₄-C at different voltages.

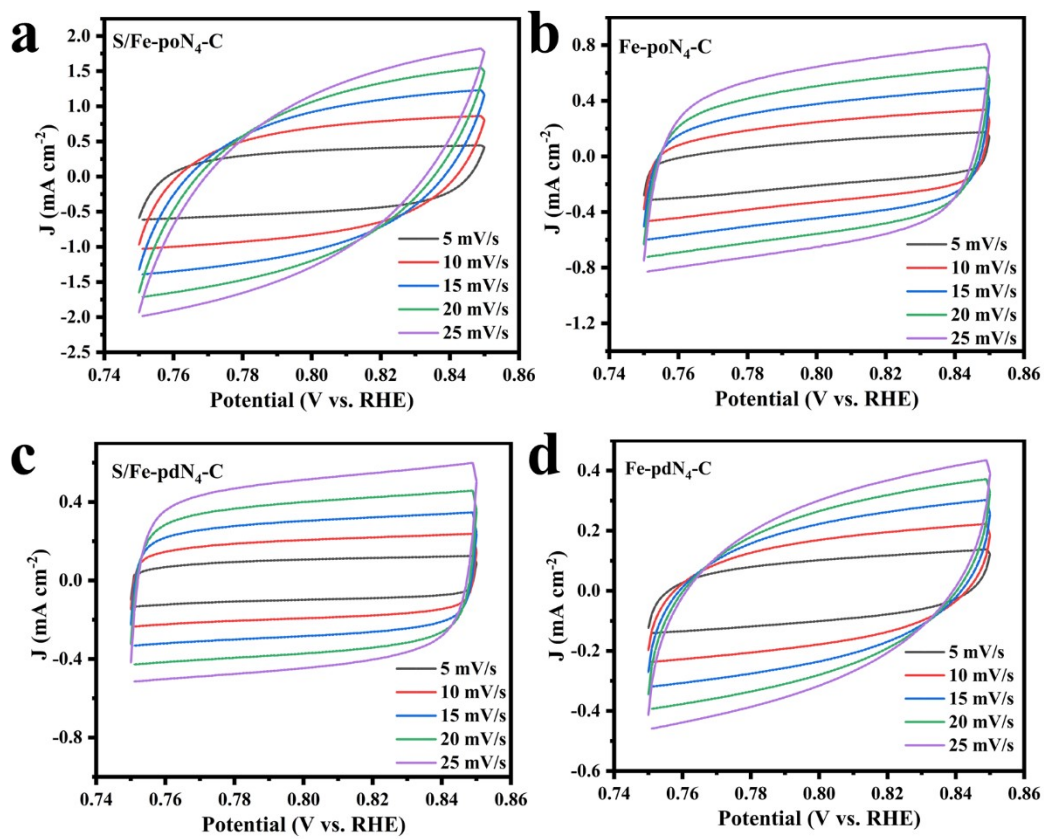


Figure S14. The CV curves at different scan rates of a) S/Fe-poN₄-C, b) Fe-poN₄-C, c) S/Fe-pdN₄-C, and d) Fe-pdN₄-C.

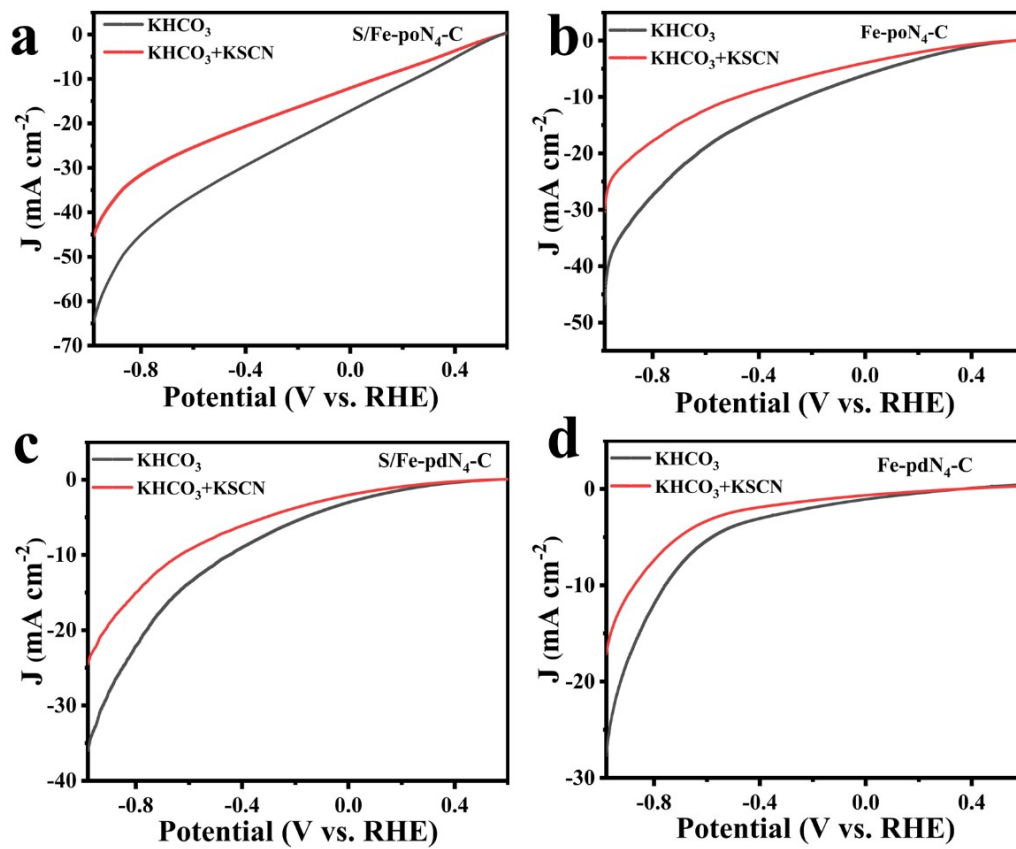


Figure S15. LSV curves of different samples in a CO₂-saturated 0.5 M KHCO₃ solution and KSCN solution. a) S/Fe-poN₄-C, b) Fe-poN₄-C, c) S/Fe-pdN₄-C, and d) Fe-pdN₄-C.

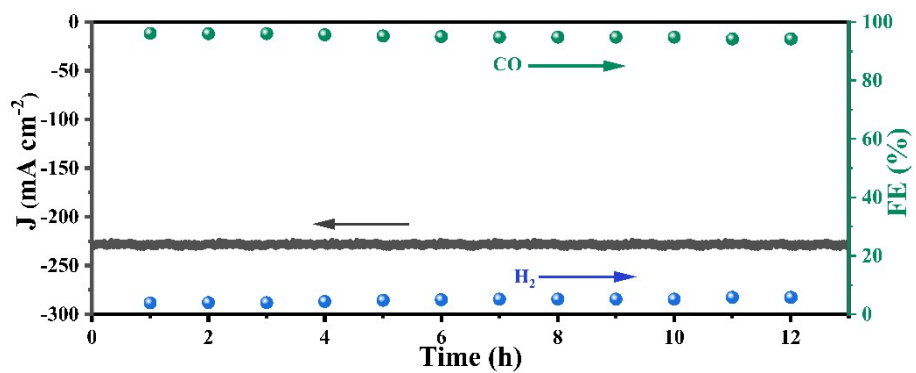


Figure S16. The long-term stability of S/Fe-poN₄-C in catalytic CO₂RR at -0.58 V vs. RHE obtained in the flow cell.

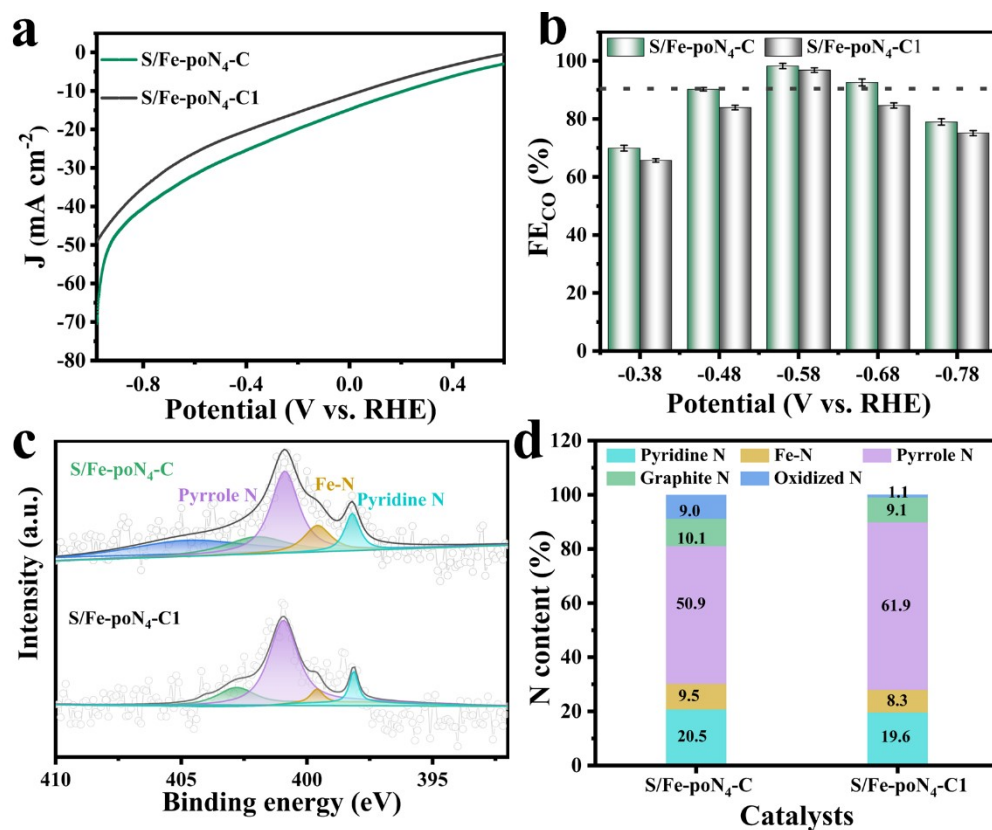


Figure S17. a) LSV plots, b) FE_{CO}, c) N 1s XPS spectra, and d) the relative contents of different N species of S/Fe-poN₄-C and S/Fe-poN₄-C1.

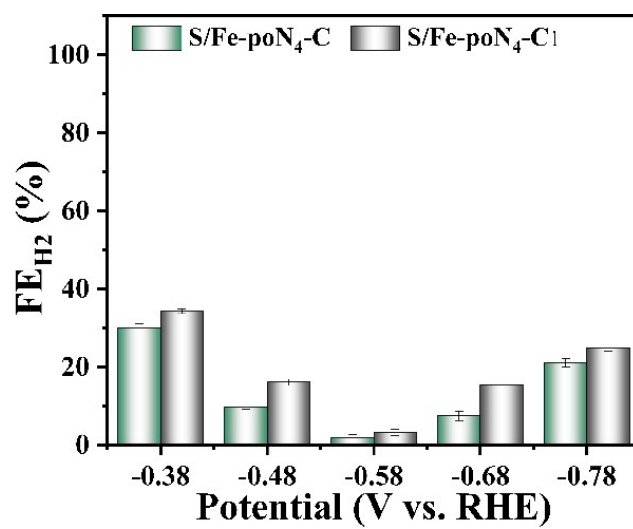


Figure S18. Faraday efficiency for hydrogen (FE_{H2}) of S/Fe-poN₄-C and S/Fe-poN₄-C1 at the varied potentials

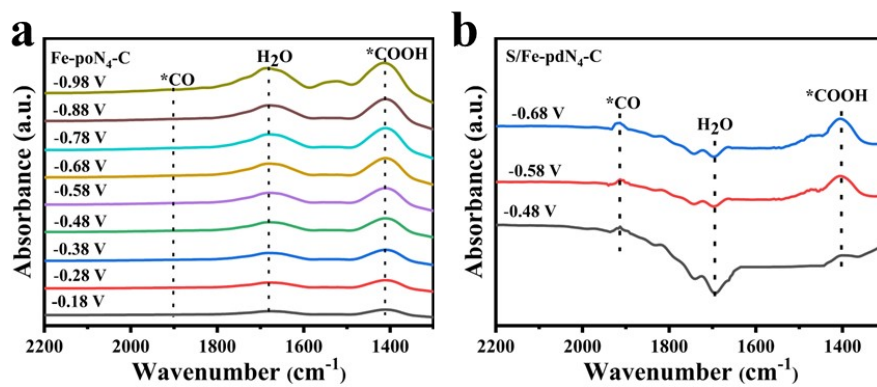


Figure S19. In-situ ATR-FTIR spectra of electrocatalytic CO₂RR with (a) Fe-poN₄-C, and (b) S/Fe-pdN₄-C.

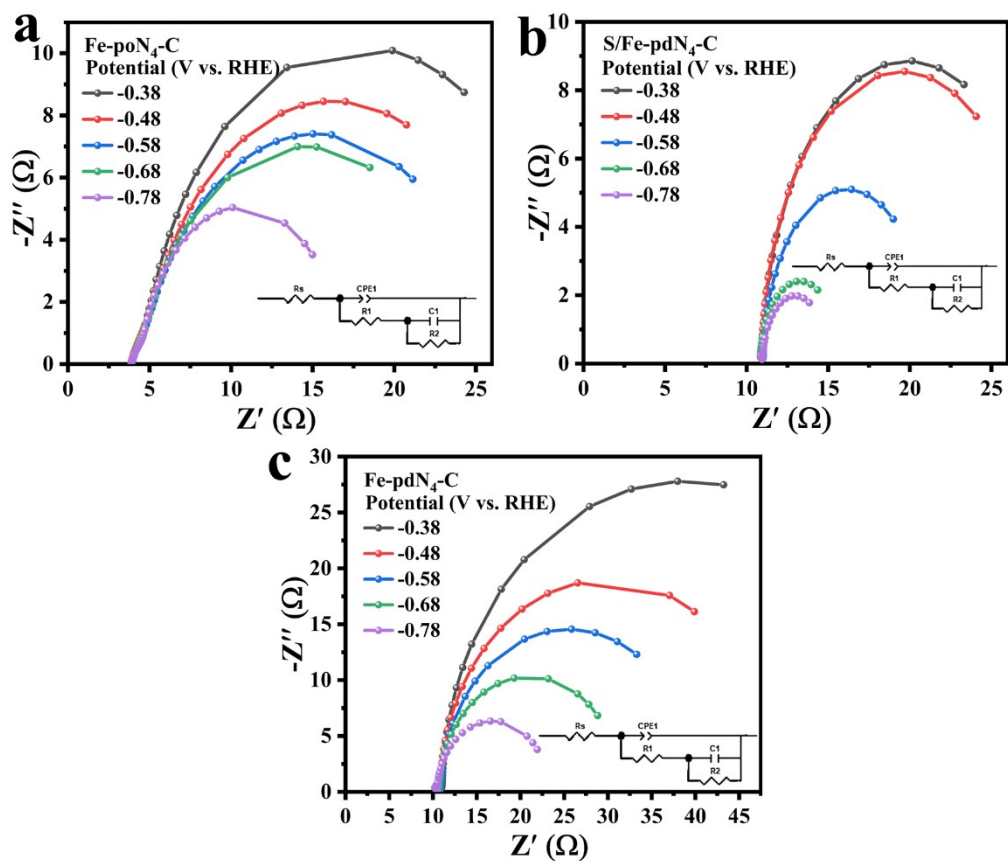


Figure S20. The EIS data and fitting results at different potentials for a) Fe-poN₄-C, b) S/Fe-pdN₄-C, and c) Fe-pdN₄-C.

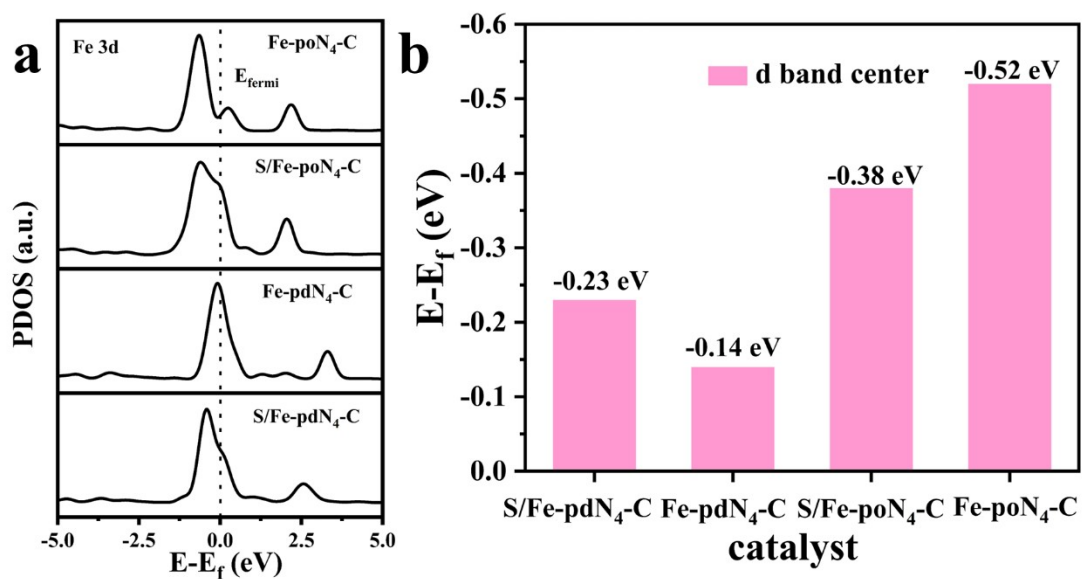


Figure S21. a) The projected density of states (PDOS) for Fe 3d orbital. b) Value of the center of the d-band.

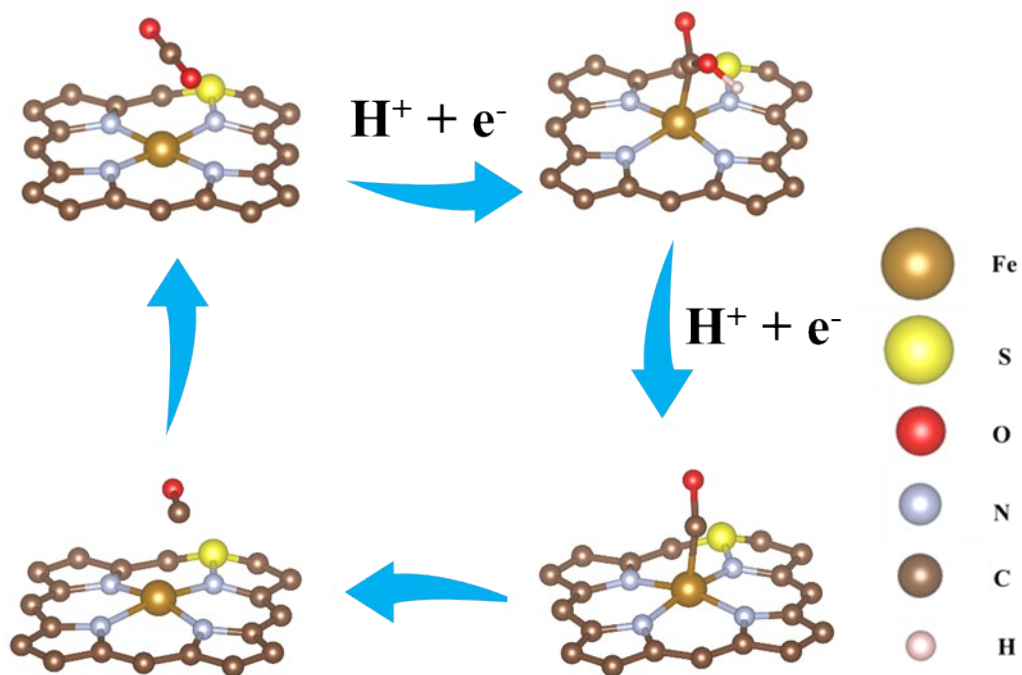


Figure S22. Reaction pathways for electrochemical CO_2 -to-CO reduction at S/Fe-poN₄-C.

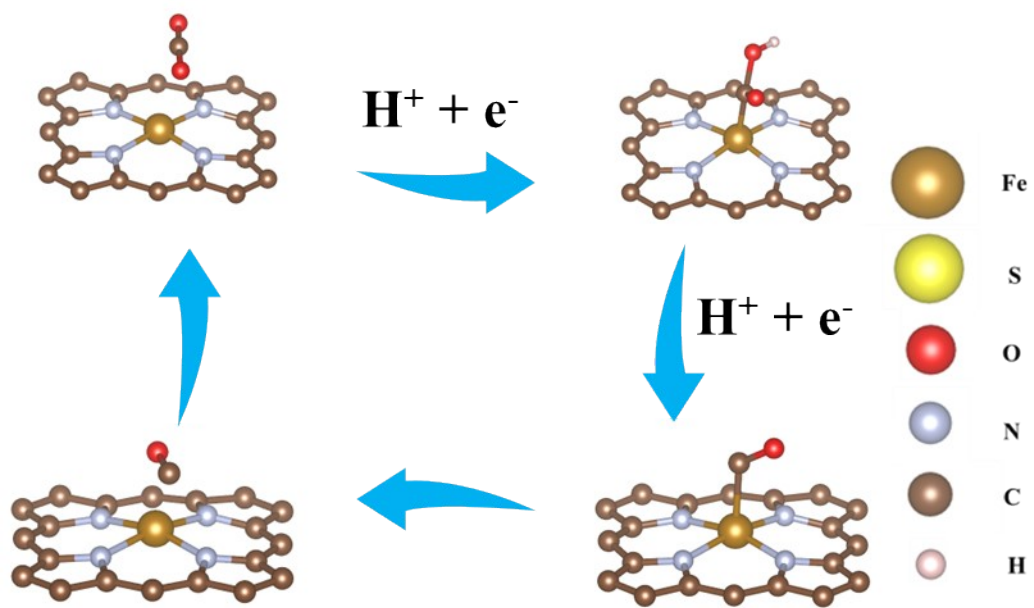


Figure S23. Reaction pathways for electrochemical CO_2 -to-CO reduction at Fe-po N_4 -C.

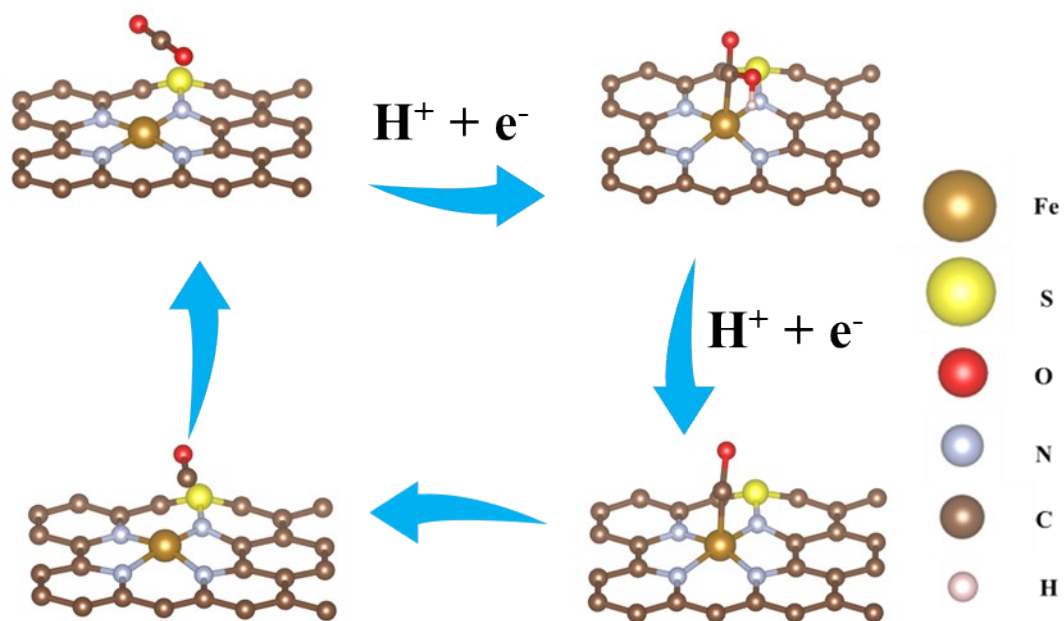


Figure S24. Reaction pathways for electrochemical CO₂-to-CO reduction at S/Fe-pdN₄-

C.

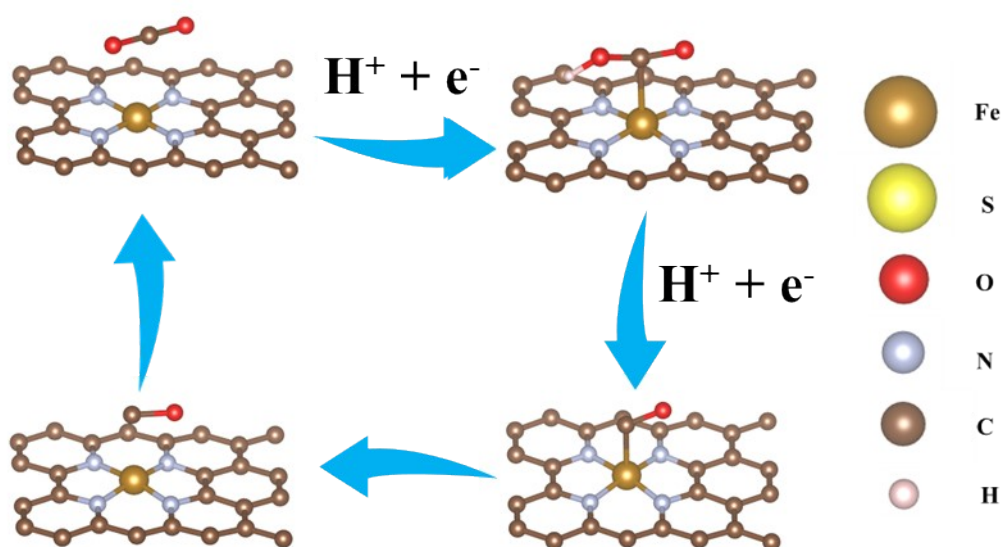


Figure S25. Reaction pathways for electrochemical CO₂-to-CO reduction at Fe-pdN₄-C.

Table S1. The Fe, N, and S elemental contents of S/Fe-poN₄-C, Fe-poN₄-C, S/Fe-pdN₄-C, and Fe-pdN₄-C.

Sample	Fe content ^a (wt.%)	N content ^b (at.%)	S content ^b (at.%)
S/Fe-poN ₄ - C	0.83	16.59	1.58
Fe-poN ₄ -C	0.92	16.04	/
S/Fe-pdN ₄ - C	0.87	16.83	1.75
Fe-pdN ₄ -C	0.72	16.87	/

^a The Fe content was determined by inductively coupled plasma-optical emission spectrometry.

^b The N and S contents were determined by CHNS elemental analysis.

Table S2. EXAFS fitting parameters at the Fe K-edge for various samples ($S_0^2=0.702$).

Sample	Shell	CN ^a	R(Å) ^b	$\sigma^2(\text{Å}^2)$ ^c	$\Delta E_0(\text{eV})$ ^d	R factor
S/Fe-poN ₄ -C	Fe-N	4.0±0.1	1.88±0.01	0.0051	7.4	0.004
S/Fe-pdN ₄ -C	Fe-N	4.1±0.1	2.11±0.01	0.0058	9.5	0.009

^a CN, coordination number; ^b R, the distance between absorber and backscatter atoms; ^c σ^2 , Debye-Waller factor to account for both thermal and structural disorders; ^d ΔE_0 , inner potential correction; R factor indicates the goodness of the fit. S_0^2 was fixed to 0.702, according to the experimental EXAFS fit of Fe foil by fixing CN as the known crystallographic value. Fitting range: $3.0 \leq k (\text{Å}) \leq 11.0$ and $1.0 \leq R (\text{Å}) \leq 3.2$ (Fe foil); $3.0 \leq k (\text{Å}) \leq 11.2$ and $1.0 \leq R (\text{Å}) \leq \sim 3.0$ (S/Fe-poN₄-C, S/Fe-pdN₄-C). A reasonable range of EXAFS fitting parameters: $0.700 < S_0^2 < 1.000$; $CN > 0$; $\sigma^2 > 0 \text{ Å}^2$; $\Delta E_0 < 10 \text{ eV}$; R factor < 0.02 .

Table S3. The fitting results of EIS at different potentials

Sample	Potential (V vs. RHE)	$R_s(\Omega)$	CPE-T	CPE-P	$R_1(\Omega)$	$R_2(\Omega)$	$C_\phi(F)$
Fe-poN ₄ -C	-0.38	3.57	0.0230	0.7847	17.80	7.54	0.0037
	-0.48	3.54	0.0194	0.8662	14.76	5.21	0.0072
	-0.58	3.49	0.0239	0.8183	13.45	4.82	0.0102
	-0.68	3.44	0.0280	0.8019	10.18	4.17	0.0124
	-0.78	3.46	0.0289	0.7882	7.06	2.03	0.0140
S/Fe-poN ₄ -C	-0.38	3.86	0.0262	0.7218	16.20	8.61	0.0065
	-0.48	3.93	0.0269	0.7218	10.44	6.41	0.0106
	-0.58	3.92	0.0282	0.7645	7.85	5.32	0.0148
	-0.68	3.91	0.0184	0.8182	6.90	4.42	0.0173
	-0.78	3.93	0.0239	0.7839	6.62	3.61	0.0190
Fe-pdN ₄ -C	-0.38	10.88	0.0226	0.9865	49.98	6.93	0.0024
	-0.48	10.7	0.0154	0.9994	36.94	5.93	0.0051
	-0.58	10.74	0.0128	0.9934	28.72	4.49	0.0072
	-0.68	10.26	0.0026	0.9101	18.04	3.23	0.0098
	-0.78	10.26	0.0030	0.9879	12.53	2.79	0.0122
S/Fe-pdN ₄ -C	-0.38	10.06	0.0395	0.9873	9.18	8.90	0.0037
	-0.48	10.12	0.0393	0.9997	9.29	7.89	0.0072
	-0.58	10.35	0.0264	1.0120	5.56	4.68	0.0102
	-0.68	10.89	0.0174	1.0090	2.15	2.69	0.0130
	-0.78	10.96	0.0209	0.9849	0.56	2.49	0.0145

Table S4. The performance comparison of S/Fe-poN₄-C with the recently reported single-atom catalysts for CO₂RR

Catalyst	FE _{CO} (%)	J _{CO} (mA/cm ²)	Potential V vs. RHE	Con. of KHCO ₃ (M)	TOF (h ⁻¹)	Ref.
S/Fe-poN₄-C	98.2	-34.2	-0.58	0.5	4621.1	This work
Fe ³⁺ -N-C	96	-20	-0.48	0.5	1000	12
Fe-N-P-C	98	-0.8	-0.34	0.5	508.8	13
Fe-N-G-P	94	-2	-0.58	0.1	1630	14
Fe ₂ NPC	96	-2.9	-0.6	0.5	3721	15
Fe-N-C-0.5	95.5	-1.9	-0.64	0.5	910	16
SAs-Ni-N-C	98.5	-5.8	-0.7	0.5	114.9	17
NiFe-DASC	94.5	-50.4	-0.8	0.5	690	18
Fe ₁ -NSC	98.6	-4.17	-0.48	0.5	1197	8
Fe ₁ NC/S ₁ - 1000	96	-6.4	-0.5	0.5	2225	19
CuN ₃ O/C	96	-1.8	-0.8	0.5	2782.6	11
Co-u- COF/graphene	93	-30	-0.74	0.5	3329	20
ZIF-NC-Ni-Fe	97.8	-18.6	-0.9	0.5	2210	21
Ni-N-C	97	-17	-0.65	0.5	3387	22
FeN ₄ Cl/NG	90.5	-10.8	-0.6	0.5	1566	23

Supplementary References

1. S. Y. Chen, X. Q. Li, C. W. Kao, T. Luo, K. J. Chen, J. W. Fu, C. Ma, H. M. Li, M. Li, T. S. Chan and M. Liu, *Angew. Chem. Int. Edit.*, 2022, **61**, e202206233.
2. E. Torres and T. P. Kaloni, *Comp. Mater. Sci.*, 2020, **171**, 109237.
3. n. Perdew, n. Burke and n. Ernzerhof, *Phys. Rev. Lett.*, 1996,**77**, 3865.
4. G. Kresse and J. Furthmüller, *Phys. Rev. B.*, 1996, **54**, 11169.
5. n. Blöchl, *Phys. Rev. B.*, 1994, **50**, 17953.
6. I. Fukuda, *J. Chem. Phys*, 2010, **129**, 164112.
7. G. S. Wu, G. C. Schatz, G. Lendvay, D. C. Fang and L. B. Harding, *J. Chem. Phys.*, 2000, **113**, 3150.
8. S. Chen, X. Li, C. W. Kao, T. Luo, K. Chen, J. Fu, C. Ma, H. Li, M. Li, T. S. Chan and M. Liu, *Angew. Chem. Int. Ed.*, 2022, **61**, e202206233.
9. W. Zheng, D. Wang, Y. Zhang, S. Zheng, B. Yang, Z. Li, R. D. Rodriguez, T. Zhang, L. Lei, S. Yao and Y. Hou, *Nano Energy*, 2023, **105**, 107980.
10. J. Chen, Z. Li, X. Wang, X. Sang, S. Zheng, S. Liu, B. Yang, Q. Zhang, L. Lei, L. Dai and Y. Hou, *Angew. Chem. Int. Ed.* 2022, **61**, e202111683.
11. W. Zheng, D. Wang, W. Cui, X. Sang, X. Qin, Z. Zhao, Z. Li, B. Yang, M. Zhong, L. Lei, Q. Zheng, S. Yao, G. Wu and Y. Hou, *Energ. Environ. Sci.*, 2023, **16**, 1007-1015.
12. J. Gu, C. S. Hsu, L. Bai, H. M. Chen and X. Hu, *Science*, 2019, **364**, 1091-1094.
13. K. Li, S. Zhang, X. Zhang, S. Liu, H. Jiang, T. Jiang, C. Shen, Y. Yu and W. Chen, *Nano Lett.*, 2022, **22**, 1557-1565.
14. F. Pan, B. Li, E. Sarnello, Y. Fei, X. Feng, Y. Gang, X. Xiang, L. Fang, T. Li, Y. H. Hu, G. Wang and Y. Li, *ACS Catal.*, 2020, **10**, 10803-10811.
15. X. Li, Y. Zeng, C. W. Tung, Y. R. Lu, S. Baskaran, S. F. Hung, S. Wang, C.-Q. Xu, J. Wang, T.-S. Chan, H. M. Chen, J. Jiang, Q. Yu, Y. Huang, J. Li, T. Zhang and B. Liu, *ACS Catal.*, 2021, **11**, 7292-7301.
16. S. Wu, X. Lv, D. Ping, G. Zhang, S. Wang, H. Wang, X. Yang, D. Guo and S. Fang, *Electrochim. Acta*, 2020, **340**, 135930.
17. J. Tuo, Y. Lin, Y. Zhu, H. Jiang, Y. Li, L. Cheng, R. Pang, J. Shen, L. Song and C. Li, *Appl. Catal. B.* 2020, **272**, 118960
18. Z. Zeng, L. Y. Gan, H. Bin Yang, X. Su, J. Gao, W. Liu, H. Matsumoto, J. Gong, J. Zhang, W. Cai, Z. Zhang, Y. Yan, B. Liu and P. Chen, *Nat. Commun.*, 2021, **12**, 4088.
19. T. Wang, X. Sang, W. Zheng, B. Yang, S. Yao, C. Lei, Z. Li, Q. He, J. Lu, L. Lei, L. Dai and Y. Hou, *Adv. Mater.*, 2020, **32**, e2002430.
20. X. Hu, Y. Liu, W. Cui, X. Yang, J. Li, S. Zheng, B. Yang, Z. Li, X. Sang, Y. Li, L. Lei and Y. Hou, *Adv. Funct. Mater.*, 2022, **33**, 2208781.
21. I. Song, Y. Eom, M. A. P, D. H. Hong, M. Balamurugan, R. Boppella, D. H. Kim and T. K. Kim, *Small*, 2023, DOI: 10.1002/sml.202300049, e2300049.

22. J. Wang, Y.-C. Huang, Y. Wang, H. Deng, Y. Shi, D. Wei, M. Li, C.-L. Dong, H. Jin, S. S. Mao and S. Shen, *ACS Catal.*, 2023, **13**, 2374-2385.
23. Z. Li, R. Wu, S. Xiao, Y. Yang, L. Lai, J. S. Chen and Y. Chen, *Chem. Eng. J.*, 2022, **430**, 132882.